

# Excitation Control of Brushless Induction Excited Synchronous Motor with Induction Machine Operating in Deep-Plugging Mode

Research paper

Amit Kumar Mondal<sup>1,\*</sup>, Saptarshi Basak<sup>2</sup>, Chandan Chakraborty<sup>1</sup>

<sup>1</sup>Indian Institute of Technology Kharagpur, Kharagpur, India

<sup>2</sup>Indian Institute of Technology Delhi, Delhi, India

Received: 12 January 2024; Accepted: 16 March 2024

**Abstract:** The popularity of electrified transportation is rising at a sharp pace due to environmental concerns over internal combustion (IC) engines. Researchers are nowadays looking for a brushless and permanent magnet (PM)-less solution for electric vehicle (EV) motors. Wound-field synchronous motor (WFSM) is a potential solution for EVs and is being used in Renault Zoe EV and BMW iX3 e-Drive models. A Brushless Induction excited Synchronous Motor (BINSYM) is a WFSM where the exciter, an induction machine (IM), is embedded inside the synchronous machine (SM) frame. Two machines (SM and IM) are configured for different numbers of poles to achieve magnetic decoupling, which facilitates independent control of both machines. The purpose of IM is to maintain the excitation requirement of SM. The IM is controlled in deep-plugging mode at a constant slip frequency over the entire speed range to minimise its reactive power demand. The maximum torque per ampere (MTPA) and root mean square (rms) current minimisation algorithms are used to control the SM. Simulation of the BINSYM-based system under dynamic conditions (MTPA with varying field current and load transient) has been carried out in MATLAB/Simulink to validate the control strategies. Experimental findings from the laboratory prototype machine closely match the simulation results.

**Keywords:** wound-field synchronous machine • brushless excitation • BINSYM • magnetic decoupling principle • EV motors

## 1. Introduction

The emphasis on transportation electrification has grown significantly over the past decade due to escalating environmental concerns. It is well-known that HV Battery forms the core of electric vehicles (EVs). Besides the HV battery, the electric motor is an important part of the drivetrain which is used for propulsion of the vehicle (Lee et al., 2021). While choosing EV motors, researchers consider various factors such as high power and torque density, efficiency, cost, ease of control, high constant power speed range (CPSR), etc. (Wang et al., 2021). Till now, permanent magnet (PM)-based motors have been widely adopted due to their advantages in terms of high torque and power density, as well as efficiency when compared to induction motor, wound-field synchronous motor (WFSM) and switched reluctance motor (SRM) (Pellegrino et al., 2012; Wang et al., 2021). However, the use of rare-earth materials (REMs) in PM-based motors poses challenges since they are sensitive to temperature variations, expensive and not uniformly available globally (Kimiabeigi et al., 2016; Raminosoa et al., 2017). PM-based motors also face issues such as PM demagnetisation over an extended speed range and reduced fault tolerance (Boldea et al., 2014). These drawbacks motivate researchers to explore alternatives to PM-based motors. Brushless WFSM emerges as a viable solution due to its superior field weakening (FW) capability and enhanced safety achieved by directly removing field excitation under faulty conditions (Park and Lim, 2019; Widmer et al., 2015).

\* Email: amitmondal@iitkharagpur.org

Various excitation systems for the WFSM have been outlined and summarised in Nøland et al. (2019). The traditional excitation system, which involves an extra exciter machine mounted on the same shaft, makes the overall system lengthy and less efficient. The exciter regulates the field current of WFSM through a rotating diode bridge rectifier (DBR), which makes the system brushless. To eliminate brushes, excitation systems utilising capacitive coupling have been developed (Dai et al., 2017; Fu et al., 2019). Due to the inability to directly sense field current in brushless synchronous motors, field current estimators have been formulated (Deriszadeh et al., 2022). Techniques for estimating rotor position have been addressed in Wang et al. (2022) and Zhang et al. (2023). Researchers have also devised methods for integrating the exciter and main machine into a single magnetic core. Several harmonic excitation schemes have been employed to provide the field excitation of WFSM (Yao et al., 2015, 2016). A spatially distributed magnetomotive force (MMF) is established in the air gap by introducing a third harmonic or DC from the stator side. The induced voltage in an additional harmonic winding placed in the rotor is rectified to supply the excitation of the main machine. Sub-harmonic excitation schemes use spatially distributed MMF of lower order harmonic by injecting currents of unequal magnitudes in two coil groups (Ali et al., 2015) or by using winding with an unequal number of turns (Ayub et al., 2019). Both harmonic and sub-harmonic excitation schemes necessitate additional control of space harmonics, leading to increased control complexity and reduced slot utilisation due to an unequal number of turns. Ongoing research explores the use of an embedded exciter, where exciter windings are positioned within power-delivering machines (Chakraborty and Rao, 2019; Dash et al., 2020; Chakraborty and Bhattacharjee, 2023). In this configuration, the exciter and the main machine (i.e. power-delivering machine) are wound with different numbers of poles to achieve magnetic decoupling, enabling independent control. The Brushless Induction excited Synchronous Generator (BINSYG) is a synchronous generator (main machine) where exciter, which is an induction machine (IM), is embedded inside the main machine. Due to its significantly lower rating compared to the main machine, the exciter can be effectively controlled by a smaller-sized converter. The performance of BINSYG in wind energy conversion systems (WECS) (Rao et al., 2021) and feeding wind power to a DC grid (Chakraborty and Bhattacharjee, 2023) at varying speeds have already been investigated. The basic control technique of BINSYG as a motor, referred to as Brushless Induction Excited Synchronous Motor (BINSYM), from zero to rated speed is reported in Dash et al. (2020). However, the literature lacks optimised utilisation and efficient control strategies for BINSYM across its wide speed range of operation. Therefore, the authors investigated to enhance the performance of BINSYM under dynamic conditions. In this paper, the CPSR of BINSYM is extended up to 3,000 rpm where the maximum speed-to-base speed ratio is 2.9. Maximum torque per ampere (MTPA) control is used for the synchronous machine (SM) with an aim to minimise the rms current of the armature winding of SM. This paper presents significant contributions in (i) the MTPA and rms current minimisation for a brushless and PM-less WFSM, considering voltage and current constraints; (ii) the control of the embedded exciter, i.e. IM, to provide the necessary field excitation over the entire speed range (zero to 3,000 rpm); (iii) the operation of the IM in deep-plugging mode to minimise its reactive power requirement; and (iv) validation of the control strategy under dynamic conditions in MATLAB simulation and laboratory prototype machine.

The article is structured into seven sections. Section 2 outlines the machine configuration and BINSYM-based system. Section 3 addresses the identification of suitable modes of operation and control of IM. The control algorithm of SM is discussed in detail in Section 4. Simulation results from MATLAB/SIMULINK under dynamic conditions are presented in Section 5. Section 6 reports the experimental results obtained from a laboratory prototype machine. Finally, Section 7 is the conclusion of the overall work.

## 2. System Description

BINSYM consists of two machines (SM and IM) embedded in a single magnetic core, and the windings of both machines share the same slots. Being power-delivering machine, SM drives the load at desired speed. The purpose of the IM is to render the field excitation requirement of SM. The layout of BINSYM is shown in Figure 1(a). SM is wound for four numbers of poles ( $p_{SM}$ ). Concentric field winding is wound on the rotor and 3-phase distributed armature winding is on the stator. IM windings are wound for six numbers of poles ( $p_{IM}$ ) to achieve magnetic decoupling. Three-phase distributed windings are incorporated for both stator and rotor windings of IM. The block diagram of the complete BINSYM-based system is shown in Figure 1(b). A rotating DBR placed on the shaft connects the 3-phase rotor winding of IM to the concentric field winding of SM, which makes the system brushless. Three-phase rotor voltage of IM is rectified to supply DC field current of SM. An inverter (Inv-1) is connected to the

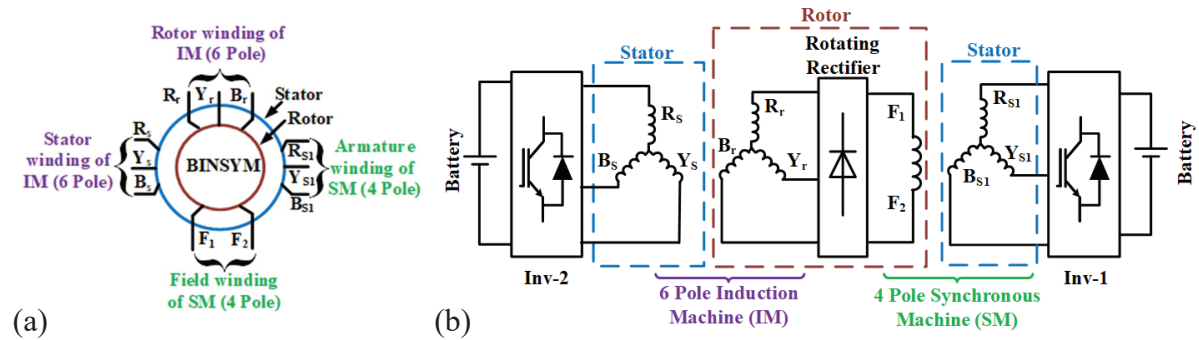


**Figure 1.** (a) Layout of BINSYM and (b) System configuration of BINSYM. BINSYM, Brushless Induction excited Synchronous Motor; IM, induction machine; SM, synchronous machine.

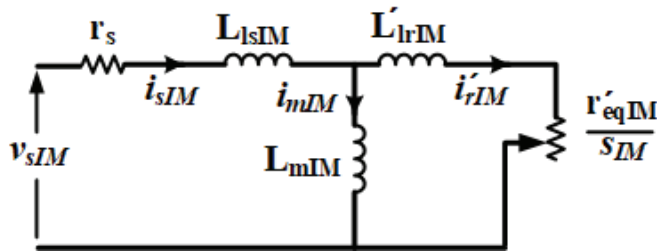


**Figure 2.** Per phase equivalent circuit of IM. IM, induction machine.

SM armature winding to feed the right amount of current at a desired frequency such that the machine can drive the load. Another inverter (Inv-2) controls the stator current of IM to maintain the excitation demand of SM under varying speed conditions.

### 3. Operating Mode and Control Strategy of IM

The shaft speed of BINSYM ( $N_r$  in rpm) is controlled by the armature current frequency of SM. Under varying shaft speed, IM must be controlled in such a way that field current of SM ( $i_{fd}$ ) is maintained constant at rated value of 1.33 A. The steady-state characteristics of IM by varying stator frequency of IM ( $f_{eIM}$ ) have been analysed for two extreme speeds (0 rpm and 3,000 rpm). The analysis is based on the per-phase equivalent circuit in Figure 2 and the ratings and parameters from Table 1. The equivalent rotor resistance of IM referred to the stator side is given by Eq. (1) (Chakraborty and Rao, 2019).

$$r'_{eqIM} = N_{srIM}^2 \left( r_{rIM} + \frac{r_{fSM}}{2} \right) \quad (1)$$

Analysis is carried out keeping  $i_{fd}$  fixed at 1.33 A, as well as the stator current of IM ( $I_{sIM}$ ) within the rated value of 4 A. Relevant steady-state characteristics of such studies are presented in Figure 3. At 0 rpm, there is a dead zone around  $f_{eIM} = 0$  Hz where  $i_{fd}$  shown in Figure 3(a) cannot be maintained at 1.33 A (keeping  $I_{sIM}$  shown in Figure 3(b) below 4 A). Slip frequency of IM is low in this dead zone. Therefore, it is challenging to induce sufficient voltage on the rotor that is necessary to achieve rated field current. Similarly, there is a dead zone around  $f_{eIM} = 150$  Hz at a shaft speed of 3,000 rpm. Operation of IM in this zone is thus restricted. Depending upon the slip of IM ( $s_{IM}$ ), there are three possible modes of operation, namely motoring, generating and plugging, in which IM can be operated to supply the excitation requirement of SM. The operating modes at 3,000 rpm shaft speed are summarised in Table 2. IM operates in plugging mode for negative stator frequency ( $s_{IM} > 1, \forall f_{eIM} < 0$  Hz). IM operates in generating mode for stator frequency of 0–150 Hz ( $s_{IM} < 0, \forall 0 \text{ Hz} < f_{eIM} < 150$  Hz). Above 150 Hz, IM is in motoring mode of operation ( $1 < s_{IM} < 0, \forall f_{eIM} > 150$  Hz). As the stator frequency of IM moves away on the sideways of dead zone in both directions,

**Table 1.** Ratings and parameters of BINSYM.

Rating or parameters of SM		Rating or parameters of IM	
Rated power, S	5 kVA	Rated power, $S_{IM}$	750 VA
Rated voltage, $V_s$	415 V	Rated voltage, $V_{sIM}$	110 V
Magnetizing inductance, $L_{mS}$	108 mH	Magnetizing inductance, $L_{mIM}$	18.7 mH
Stator leakage inductance, $L_{ls}$	2.1 mH	Stator leakage inductance, $L_{lsIM}$	1.64 mH
Field leakage inductance, $L_{lSM}$	3.7 mH	Rotor leakage inductance, $L_{lrIM}$	1.64 mH
Stator resistance, $r_s$	1.3 $\Omega$	Stator resistance, $r_{sIM}$	2.1 $\Omega$
Field resistance, $r_{fSM}$	41 $\Omega$	Rotor resistance, $r_{rIM}$	3.5 $\Omega$
Field to stator turns ratio, $N_{fs}$	11.26	Stator to rotor turns ratio, $N_{srIM}$	1.02

BINSYM, Brushless Induction excited Synchronous Motor; IM, induction machine; SM, synchronous machine.

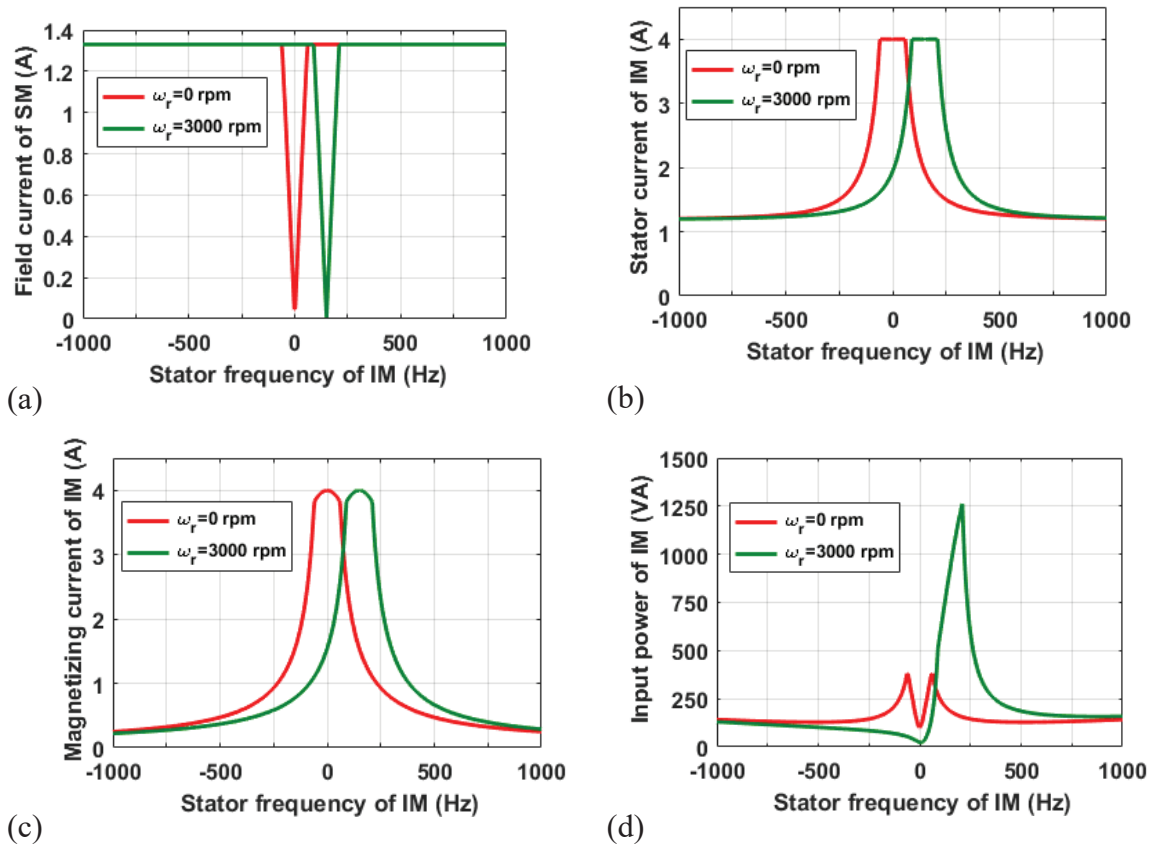


**Figure 3.** Steady-state characteristics of IM at 0 rpm and 3,000 rpm: (a) Field current of SM, (b) Stator current of IM, (c) Magnetising current of IM and (d) Input power of IM. IM, induction machine; SM, synchronous machine.

**Table 2.** Operational modes of IM with variable stator frequency at 3,000 rpm shaft speed.

Rotor current frequency ( $f_{rIM}$ )	Stator current frequency ( $f_{sIM}$ )	Slip ( $s_{IM}$ )	Operating mode
-250 Hz	$f_{sIM} < 0$	$s_{IM} > 1$	Plugging
-250 Hz	$0 \text{ Hz} < f_{sIM} < 150 \text{ Hz}$	$s_{IM} < 0$	Generating
-250 Hz	$f_{sIM} > 150 \text{ Hz}$	$1 < s_{IM}$	Motoring

IM, induction machine.

the magnetising current required for the IM decreases as per Figure 3(c). The apparent power drawn by the IM has been shown in Figure 3(d). Volt-ampere input to IM at standstill condition remains almost the same irrespective of the sign of stator frequency. But at 3,000 rpm, the volt-ampere input of IM is considerably high if IM is operated in the motoring mode rather than plugging mode. It is intended to operate IM at reduced magnetising current as well as low input power. Therefore, it is suitable to control the IM in the plugging mode for the entire speed range of BINSYM. It is evident from Figure 3(c) that the decrement of magnetising current at standstill condition is not significant for  $f_{eIM} \leq 250$  Hz, but it will increase the core losses. Slip frequency in this case is  $-250$  Hz. Similarly, for a shaft speed of 3,000 rpm, the decrement of magnetising current is not significant for  $f_{eIM} \leq 100$  Hz. Slip frequency corresponding to  $f_{eIM} = -100$  Hz and 3,000 rpm of speed is  $-250$  Hz. A similar explanation is applicable for different speeds also. Therefore, slip frequency of IM is maintained constant at  $-250$  Hz over the entire speed range of BINSYM. A constant slip frequency control algorithm is used to control the IM such that it can maintain rated field current of IM. Since the stator frequency of IM varies from  $-250$  Hz to  $-100$  Hz (which is much less than zero), it is mentioned that IM is operated in deep-plugging mode (Chakraborty and Bhattacharjee, 2023).

The rotor terminals of IM are connected to field winding of SM through a DBR. Therefore, fundamental component

of per phase rotor current of IM is  $I'_{rIM} = \sqrt{\frac{2}{3}} \frac{i_{fd}}{N_{srIM}}$ . The dq-axis rotor flux linkage of IM is given by Eqs. (2) and (3).

$$\lambda'_{qrIM} = L'_{lrIM} i'_{qrIM} + L_{mIM} (i_{qsIM} + i'_{qrIM}) \quad (2)$$

$$\lambda'_{drIM} = L'_{lrIM} i'_{drIM} + L_{mIM} (i_{dsIM} + i'_{drIM}) \quad (3)$$

Rotor flux-oriented control has been used to control the IM so that  $i_{fd}$  is directly proportional to q-axis stator current of IM ( $i_{qsIM}$ ) as per Eq. (4). To do so, rotor flux linkage of IM ( $\lambda'_{qrIM}$ ) is made equal to zero. The flux component of current of IM ( $i_{dsIM}$ ) is calculated from Eq. (5).

$$i_{qsIM} = -\frac{L_{rIM}}{L_{mIM}} i'_{qrIM} = -\frac{L_{rIM}}{L_{mIM}} \frac{2}{\sqrt{3}} \frac{i_{fd}}{N_{srIM}} \quad (4)$$

$$\omega_{sIM} = -\frac{i_{qsIM} r'_{eqIM}}{i_{dsIM} L_{rIM}} \Rightarrow i_{dsIM} = -\frac{i_{qsIM} R'_{eqIM}}{\omega_{sIM} L_{rIM}} \quad (5)$$

where  $L_{rIM} = L_{mIM} + L'_{lrIM}$ .

As slip frequency of IM ( $\omega_{sIM}$  rad/s) is constant,  $i_{dsIM}$  is directly proportional to  $i_{qsIM}$ . The rotor current of IM is controlled through Inv-2 (shown in Figure 1(b)) by varying the stator frequency ( $f_{eIM}$ ) and q-axis current ( $i_{qsIM}$ ) of IM under varying shaft speeds. As  $i_{fd}$  is maintained at a fixed value and constant slip frequency control technique is adopted for IM,  $i_{qsIM}$  and  $i_{dsIM}$  calculated from Eqs. (4) and (5) always remain constant.

## 4. Control Strategy of SM and Controller of BINSYM

### 4.1. Torque capability of SM based on boundary conditions

The field-oriented control algorithm is implemented for SM to satisfy the torque and speed demand of the load. The steady-state operation of SM must be within the continuous ratings provided in Table 1. Based on the rated value, the armature current limit of SM will give an equation of circle (I-circle) with a centre at the origin and radius of  $I_{sm}$  as described in Eq. (6). The steady-state d-axis and q-axis currents of SM are  $i_{ds}$  and  $i_{qs}$ , respectively. The peak value of line current of SM is  $I_{sm}$ .

$$i_{qs}^2 + i_{ds}^2 \leq I_{sm}^2 \quad (6)$$

Steady-state q-axis voltage ( $v_{qs}$ ) and d-axis voltage ( $v_{ds}$ ) are given in Eqs. (7) and (8), respectively. Torque developed by SM ( $T_e$ ) is as per Eq. (9). Having a cylindrical rotor structure, synchronous inductance of SM are

$L_d \approx L_q = L_{ls} + L_{md}$ . The rotor speed of SM (or shaft speed) is  $\omega_r$  rad/s (electrical). Field current referred to stator is given by  $i'_{fd} = \frac{2}{3} N_{fs} i_{fd}$ .

$$v_{qs} = r_s i_{qs} + \omega_r L_d i_{ds} + \omega_r L_{md} i'_{fd} \quad (7)$$

$$v_{ds} = r_s i_{ds} - \omega_r L_q i_{qs} \quad (8)$$

$$T_e = \frac{3}{2} \frac{p_{SM}}{2} L_{md} i'_{fd} i_{qs} \quad (9)$$

Like I-circle, the voltage boundary (V-circle) is also decided by the peak value of per phase rated armature voltage ( $V_{sm}$ ) as per Eq. (10). This boundary condition constructs a circle with a centre at  $\left( V_x = -\frac{\omega_r^2 L_q L_{md} i'_{fd}}{r_s^2 + (\omega_r L_d)^2}, V_y = -\frac{r_s \omega_r L_{md} i'_{fd}}{r_s^2 + (\omega_r L_d)^2} \right)$  and a radius of  $r_V = \frac{V_{sm}}{\sqrt{r_s^2 + (\omega_r L_d)^2}}$ .

$$v_{qs}^2 + v_{ds}^2 \leq V_{sm}^2$$

$$\Rightarrow (i_{ds} - V_x)^2 + (i_{qs} - V_y)^2 \leq r_V^2 \quad (10)$$

The I-circle is independent of speed. For a constant  $i_{fd}$ , V-circles are concentric circles whose radius reduces with an increase in speed. The SM must be operated on or inside the V-circle and the I-circle: the common area inside the circles is the safe operating area (SOA) of SM. The base speed of SM ( $\omega_{rb}$ ), up to which rated torque can be developed, is calculated by putting  $i_{qs} = I_{sm}$  and  $i_{ds} = 0$  in Eq. (10). The expression of  $\omega_{rb}$  given in Eq. (11) is found to be 1,030 rpm.

$$\omega_{rb} = \frac{-r_s L_{md} i'_{fd} I_{sm} + \sqrt{a_1^2 - b_1^2 + c_1^2}}{(L_{md} i'_{fd})^2 + (L_d I_{sm})^2} \quad (11)$$

where  $a_1 = L_{md} i'_{fd} V_{sm}$ ,  $b_1 = r_s L_d I_{sm}$  and  $c_1 = L_d I_{sm} V_{sm}$

SM can develop rated torque of  $T_e = 31.6$  N·m at  $i_{qs} = 9.85$  A in constant torque region (zero to base speed) as shown in Figure 4(a) where  $i_{ds}$  is maintained at zero. In the FW region, maximum torque that can be extracted from

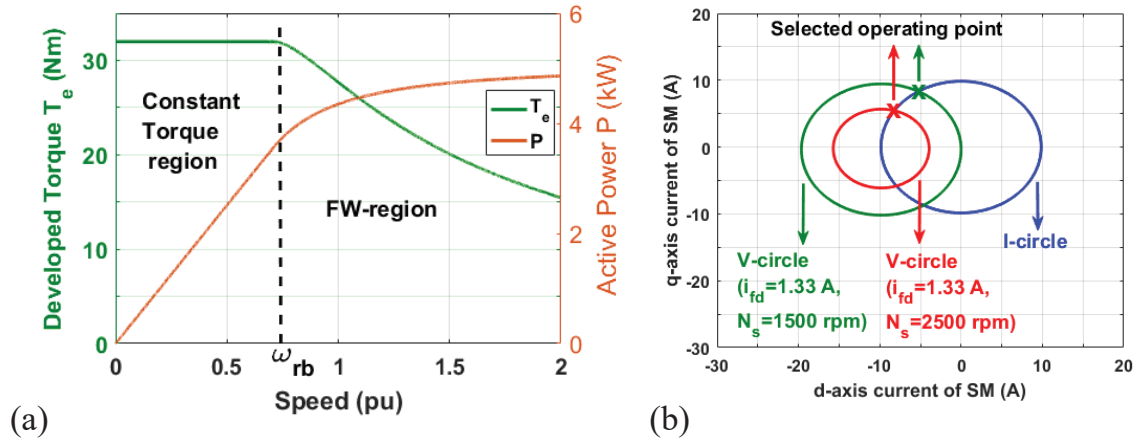


**Figure 4.** (a) Torque developed and power of SM at varying speed, (b) Operating points in circle diagram corresponding to maximum torque at 1,500 rpm and 2,500 rpm. SM, synchronous machine.

SM reduces with an increase in speed. The  $i_{qs}$  must be maximum to extract maximum torque from the SM following the torque equation in Eq. (9). Therefore,  $i_{qs}$  is calculated from the intersection point of V-circle and I-circle and it is given by Eq. (12).

$$a_1 i_{qs}^2 + b_1 i_{qs} + c_1 = 0$$

$$\Rightarrow i_{qs} = \frac{-b_1 + \sqrt{b_1^2 - 4a_1 c_1}}{2a_1} \quad (12)$$

where  $a_1 = (2r_s \omega_r L_{md} i'_{fd})^2 + (2\omega_r^2 L_d L_{md} i'_{fd})^2$ ,  $b_1 = 4r_s \omega_r L_{md} i'_{fd} \left( (\omega_r L_{md} i'_{fd})^2 + (\omega_r L_d I_{sm})^2 + (r_s I_{sm})^2 - V_{sm}^2 \right)$  and  $c_1 = \left( (\omega_r L_{md} i'_{fd})^2 + (\omega_r L_d I_{sm})^2 + (r_s I_{sm})^2 - V_{sm}^2 \right) - (2\omega_r^2 L_d L_{md} i'_{fd} I_{sm})^2$ .

In the FW region,  $i_{ds}$  is calculated by  $-\sqrt{I_{sm}^2 - i_{qs}^2}$  to extract maximum torque at rated voltage. The operating points for maximum achievable torque at a speed of 1,500 rpm and 2,500 rpm are shown in the circle diagram in Figure 4(b).

## 4.2. MTPA control by varying field current

One of the major objectives of this work is to achieve MTPA control and minimise the rms current of armature winding of SM. The MTPA control can be achieved below base speed by maintaining  $i_{ds} = 0$  which minimises armature current. In the FW region, depending on speed and load, the injection of negative value of  $i_{ds}$  may be required to confine the voltage within rated value. Considering voltage and current boundary conditions, the effect of field current control on the developed torque in the FW region is explored in this subsection. The field current of SM is chosen to achieve maximum torque value per ampere (TPA).

$$TPA = \frac{T_e}{i_s} = \frac{T_e}{\frac{1}{\sqrt{2}} \sqrt{i_{qs}^2 + i_{ds}^2}} \quad (13)$$

For a particular value of torque and field current, the value of  $i_{qs}$  is calculated from Eq. (9). If  $i_{fd}$  is reduced,  $i_{qs}$  increases to maintain the torque. The operating point is chosen to be on the voltage circle which minimise the  $i_{ds}$  and hence maximise TPA. The value of  $i_{ds}$  is calculated by solving Eq. (10) and it is given by Eq. (14). Any positive value of  $i_{ds}$  is not considered as it will saturate the magnetic core of the machine and increase armature current as well.

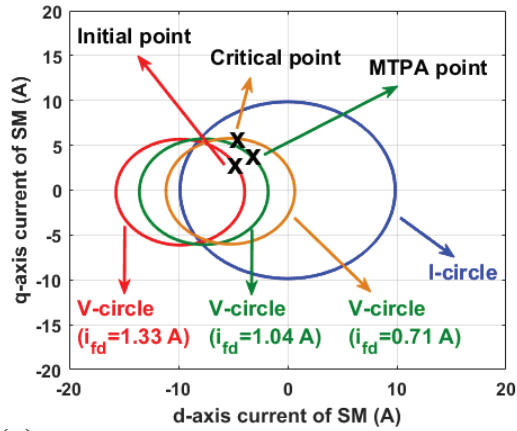
$$a_2 i_{ds}^2 + b_2 i_{ds} + c_2 = 0$$

$$\Rightarrow i_{ds} = \frac{-b_2 + \sqrt{b_2^2 - 4a_2 c_2}}{2a_2} \quad (14)$$

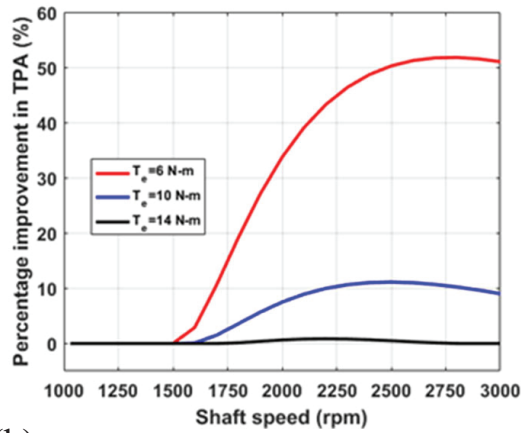
where  $a_2 = r_s^2 + (\omega_r L_d)^2$ ,  $b_2 = 2\omega_r^2 L_d L_{md} i'_{fd}$  and  $c_2 = (\omega_r L_d i_{qs})^2 + (r_s i_{qs})^2 + (\omega_r L_{md} i'_{fd})^2 + 2r_s \omega_r L_{md} i'_{fd} i_{qs} - V_{sm}^2$ .

Referring to circle diagram at a speed of 2,500 rpm in Figure 5(a), initial operating point is marked where  $i_{fd} = 1.33$  A,  $i_{qs} = 3.085$  A,  $i_{ds} = -4.93$  A,  $i_s = 4.11$  A and  $TPA = 2.43$  N·m/A. Field current can be reduced up to 0.71 A, which eventually increase  $i_{qs}$  to 5.78 A, where operating point marked as critical point in Figure 5(a) is on the positive maximum point on the V-circle. However, it is found that  $i_s$  (3.708 A) is minimum for a field current of 1.04 A where TPA is maximum at 2.7 N·m/A. The armature currents of SM at MTPA operating point are  $i_{qs} = 3.94$  A,  $i_{ds} = -3.46$  A and  $i_s = 3.708$  A.

The MTPA in the FW region for different values of torques (6 N·m, 10 N·m, 14 N·m, 18 N·m) are plotted in Figure 6(a). The field current shown in Figure 6(b) depicts that for light load, field current need to be reduced after certain speed to achieve MTPA. It is found that as the torque increases, MTPA can be achieved near rated field current. For a particular value of torque,  $i_{qs}$  current in Figure 6(c) increases as field current decreases. As the speed increases, as shown in Figure 6(d), negative value of  $i_{ds}$  need to be injected to operate the SM within rated voltage.

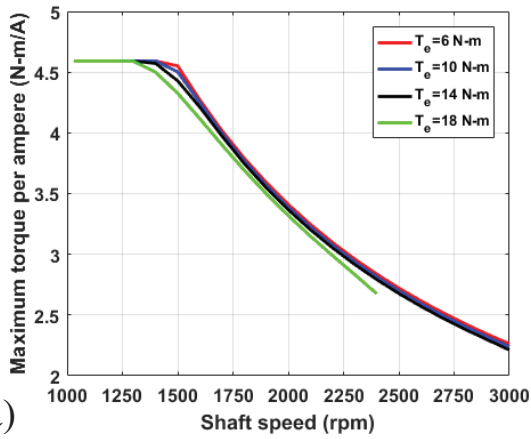


(a)

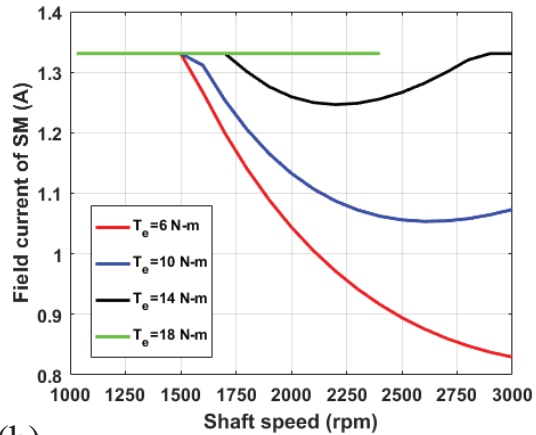


(b)

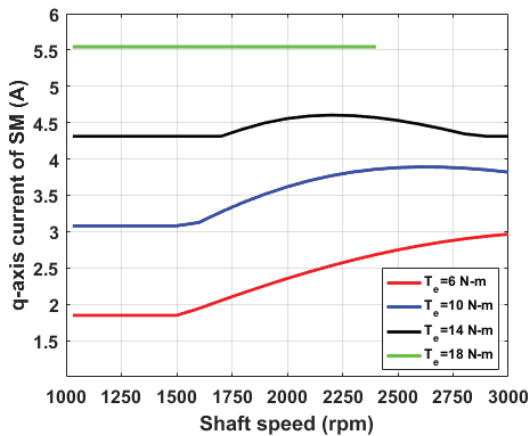
**Figure 5.** (a) Operating point to achieve MTPA by varying field current for 10 N m of torque at a speed of 2,500 rpm, (b) percentage improvement in values of MTPA by varying field current. MTPA, maximum torque per ampere; SM, synchronous machine.



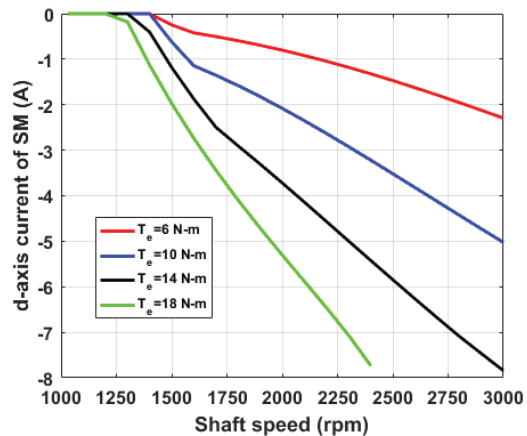
(a)



(b)



(c)



(d)

**Figure 6.** (a) MTPA, (b) field current, (c) d-axis current, (d) q-axis current of SM for different values of torque. MTPA, maximum torque per ampere; SM, synchronous machine.

Considering the voltage and current limits, the BINSYM under consideration is unable to develop a torque of 18 N·m above a speed of 2,400 rpm. Therefore, the MTPA curves are truncated at 2,400 rpm for a torque output of 18 N·m. The percentage improvement in MTPA by controlling the field current compared to operation at rated field current is shown in Figure 5(b). It is found that MTPA can be enhanced as high as 51% for 6 N·m of torque at a speed of 2,800 rpm.

### 4.3. Description of controller of BINSYM

The overall controller block diagram of SM and IM, along with BINSYM, has been shown in Figure 7. The controller of SM has been implemented in such a way that the shaft speed of the BINSYM is maintained as per the reference speed  $\omega_r^*$ . Actual speed and the rotor angle of SM are estimated by back-emf-based sensorless control (Wang et al., 2012). Two back-to-back proportional integral (PI) controllers generate q-axis reference current  $i_{qs}^*$  and q-axis reference voltage  $v_{qs}^*$  based on speed error and current error signal, respectively. The d-axis reference current  $i_{ds}^*$  is generated based on the MTPA or rms current minimisation algorithm discussed in Section 4.1. The third harmonic injected sinusoidal pulse width modulation (SPWM) technique is used to generate gate pulses for Inv-1. The q-axis and d-axis current reference of IM  $i_{qsIM}^*$  and  $i_{dsIM}^*$  are kept constant as per Eqs. (4) and (5), respectively. These values of IM currents maintain the excitation requirement of SM. Rotor speed of IM  $\omega_{rIM}$  is related to shaft speed by  $\omega_{rIM} = \frac{p_{IM}}{2} \omega_r$ . Two PI controllers generate dq-axis voltage references  $v_{dsIM}^*$  and  $v_{qsIM}^*$ . In case of IM also, third harmonic injected SPWM technique is used to generate gate pulses for Inv-2.

## 5. Simulation Results

The simulation studies of BINSYM under dynamic conditions have been conducted in MATLAB/Simulink platform. The parameters and ratings of IM and SM are taken from Table 1. Performance of BINSYM under MTPA control,

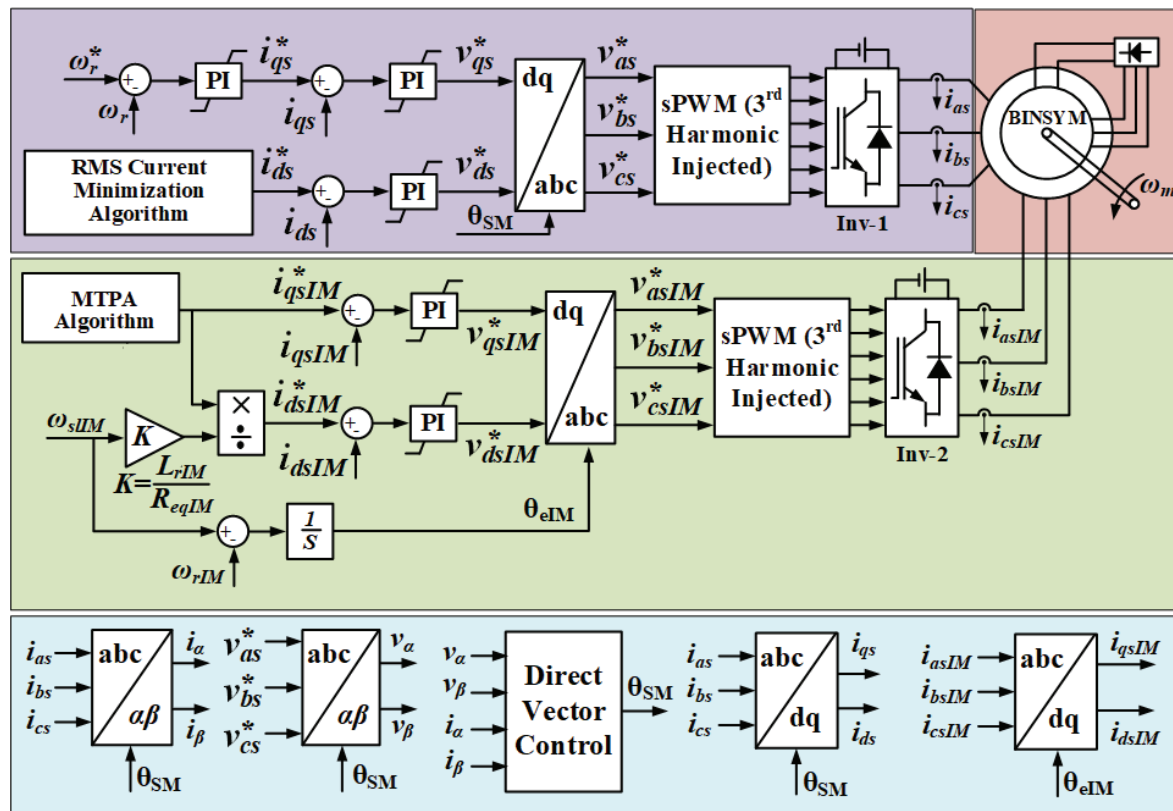


**Figure 7.** Block diagram of overall BINSYM controller. BINSYM, Brushless Induction excited Synchronous Motor; IM, induction machine; MTPA, maximum torque per ampere; PI, proportional integral.

load transient has been studied. IM controller ensures that it can control the field current of SM under these dynamic conditions.

### 5.1. MTPA control under constant and variable field current

In this study, field current of SM is reduced from the rated value of 1.33 A to achieve MTPA for 10 N·m of torque at a shaft speed of 2,500 rpm. The reference shaft speed and torque, shown in Figure 8(a), are maintained constant throughout the study. Refer to Figure 8(b), initially, field current is at 1.33 A and TPA is 2.43 N·m/A. At 45 s, MTPA control is activated. As a result, field current starts decreasing and reaches 1.04 A at 48.5 s where TPA attains the maximum value of 2.7 N·m/A. The dq-axis currents of IM are shown in Figure 8(c). During transient condition,  $i_{qsIM}$  changes from -1.64 A to -1.282 A to control the field current of SM precisely. The  $i_{dsIM}$  reduces from 1.28 A to 1 A to maintain excitation of IM. As the shaft speed is constant at 2,500 rpm, stator frequency is fixed at -125 Hz for a constant slip frequency of -250 Hz as shown in Figure 8(c). As the field current decreases to achieve MTPA,  $i_{qs}$ , shown in Figure 8(d), increases from 3.085 A to 3.94 A to maintain the torque at 10 N·m. The  $i_{ds}$  is initially at -4.93 A and peak value of per phase armature voltage is 340 V as shown in Figure 8(d). As the field current and q-axis current changes,  $i_{ds}$  reduces to -3.46 A while armature voltage is maintained constant at 340 V which ensures the operating point is on the V-circle. The MTPA is achieved by field current control and reducing the armature current of SM shown in Figure 8(d) from 4.11 A to 3.708 A.

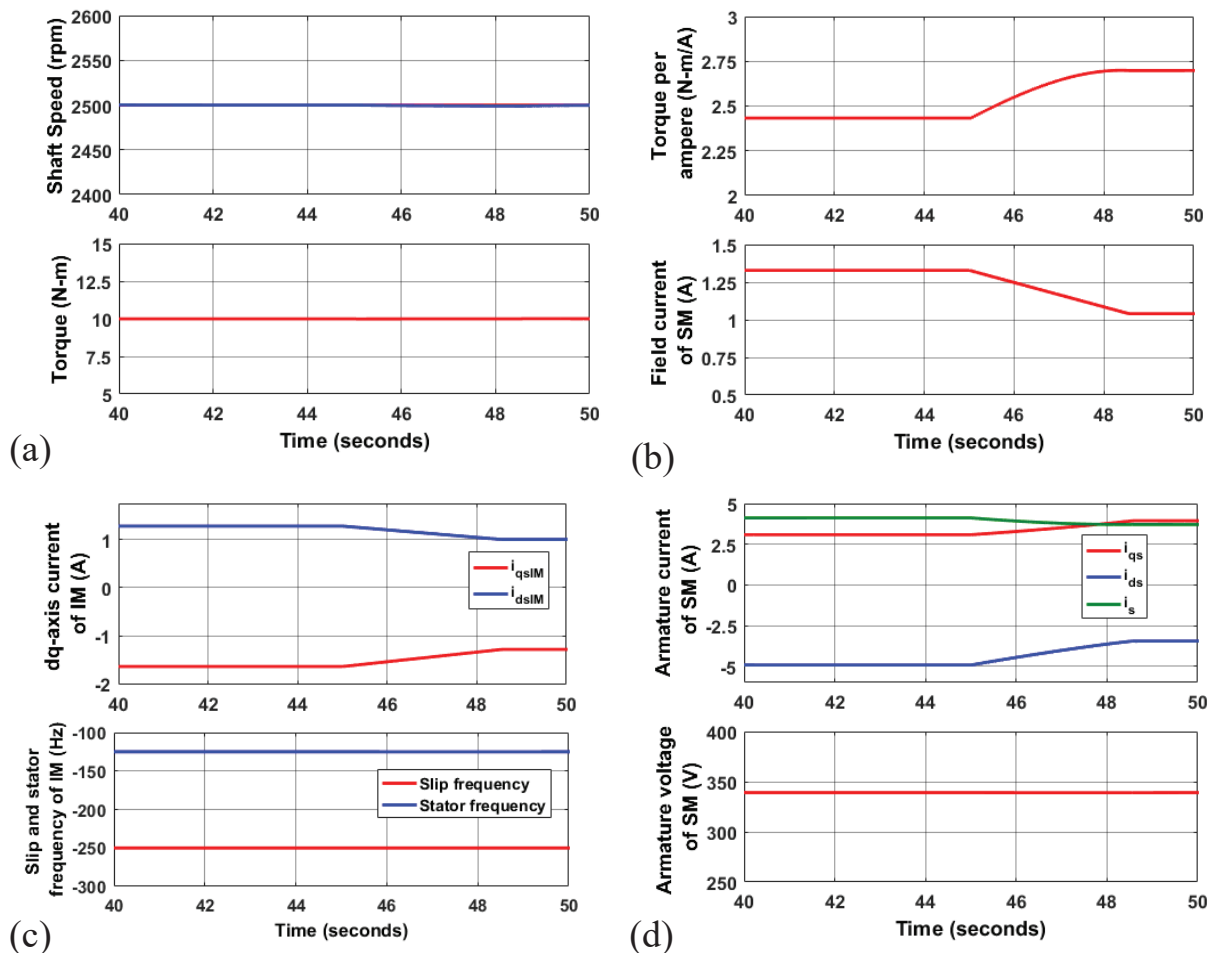


**Figure 8.** Simulation results to achieve MTPA under variable field current of SM: (a) Shaft speed and torque developed by SM, (b) TPA and field current of SM, (c) dq-axis currents, slip frequency and stator frequency of IM, (d) dq-axis currents, armature current and armature voltage of SM. IM, induction machine; MTPA, maximum torque per ampere; SM, synchronous machine; TPA, torque per ampere.

## 5.2. Load transient

The reference shaft speed is kept constant at 1,000 rpm while load is added and removed to study the performance of BINSYM under load transient condition. Initially, SM develops 22 N·m of torque at steady-state as shown in Figure 9(a). Load torque of 4.5 N·m is added and again removed at 30 s and 35 s, respectively. The torque developed by SM fulfils the load demand properly. At steady-state, actual speed is constant at 1,000 rpm but there is a maximum 1.5% change in actual speed during load transient as shown in Figure 9(a). As there is not much change in shaft speed and slip frequency of IM is maintained constant at -250 Hz, stator frequency and slip of IM remains almost constant at -200 Hz and 1.25 Hz, respectively, as per Figure 9(b). High stator frequency and slip value more than unity ensure that the IM operates in deep-plugging mode during load transient. The dq-axis currents of IM are  $i_{qsIM} = -1.63$  A and  $i_{dsIM} = 1.28$  A such that it can provide 1.33 A of rated field current of SM as shown in Figure 9(c). The controller of IM works appropriately to maintain excitation of SM under transient condition. In Figure 9(d), the  $i_{qs}$  changes from 6.8 A to 8.2 A to develop sufficient torque for an increment of 4.5 N·m of load torque while  $i_{fd}$  is maintained constant at rated value. Speed being in constant torque region,  $i_{ds}$  is maintained at zero as shown in Figure 9(d) to achieve MTPA control. Per phase peak value of armature voltage in Figure 9(d) is less than limit value ( $V_{sm}$ ). SM operates

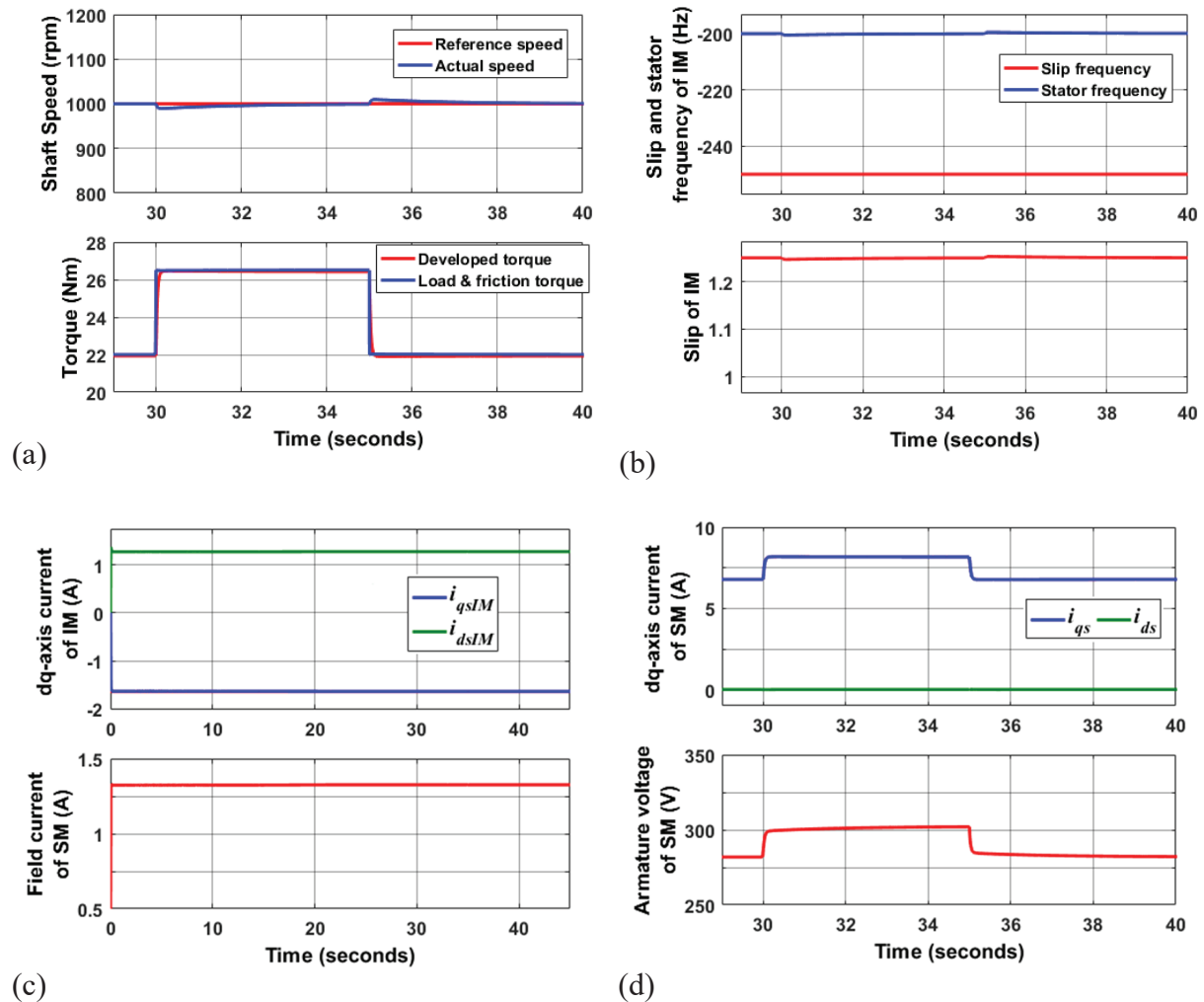


**Figure 9.** Simulation results corresponding to load change from 22 N m to 26.5 N m: (a) Shaft speed and torque developed by SM, (b) stator frequency, slip frequency and slip of IM, (c) dq-axis currents of IM and field current of SM, (d) dq-axis currents and armature voltage of SM. IM, induction machine; SM, synchronous machine.

within SOA as the armature voltage and current are within the rated value. IM operates in deep-plugging mode through constant slip frequency control and MTPA control of SM is achieved successfully under load transient.

## 6. Experimental Results

The working principle of BINSYM and the control strategies for both IM and SM are verified experimentally using laboratory prototype BINSYM. The complete BINSYM-based experimental set-up is shown in Figure 10. In the prototype machine, brushes and slip-rings are kept only for observing the voltage and current signals. No signals are taken from slip-rings to develop control logic. A DC machine mechanically coupled to the BINSYM shaft has been used as a load. All the control algorithms are implemented in the digital controller (dSPACE MicroLabBox). The pulse width modulated pulses from dSPACE MicroLabBox are fed to two inverters (Inverter for SM and Inverter for IM) through level shifter circuit and gate driver circuit. DBR connects 3-phase rotor windings of IM to field winding of SM. Relevant experimental results for load transient validate the simulation findings.

### 6.1. Load transient

BINSYM initially rotates at 1,000 rpm at steady-state condition as shown in Figure 11(a) and the reference speed is kept constant at 1,000 rpm during load transient. Load is applied at 101 s so that torque developed by SM shown in Figure 11(b) increases from 22 N·m to 26.5 N·m. The load is removed again at 117 s. Actual speed of the SM follows the reference properly. There is a change in speed of  $\pm 20$  rpm during step change in load torque.

IM stator currents are controlled such that field current of SM shown in Figure 11(c) is maintained constant at 1.33 A throughout the load transient. As per Figure 11(e), stator current of IM at steady-state condition has a frequency of  $-200$  Hz, which ensures constant slip frequency ( $-250$  Hz) operation of IM. The IM operates in plugging mode as slip of IM is 1.25 under this condition. The dq-axis currents of SM are shown in Figure 11(e). As load increases,  $i_{qs}$  increases from 6.8 A to 8.2 A to support the load torque while maintaining speed. The shaft speed being below base speed,  $i_{ds}$  current remains constant at 0 A. Three-phase steady-state currents of SM at  $T_e = 26.5$  N·m are presented in Figure 11(f) which has a peak value of 8.2 A (same as  $i_{qs}$ ).

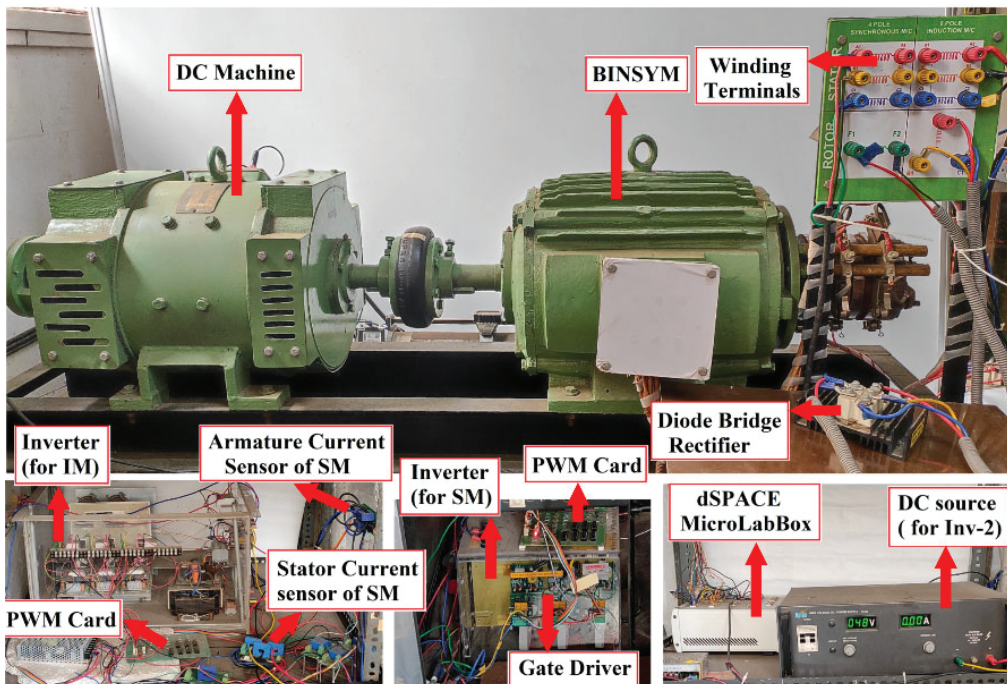


**Figure 10.** Experimental set-up of BINSYM-based system. BINSYM, Brushless Induction excited Synchronous Motor; IM, induction machine; SM, synchronous machine.

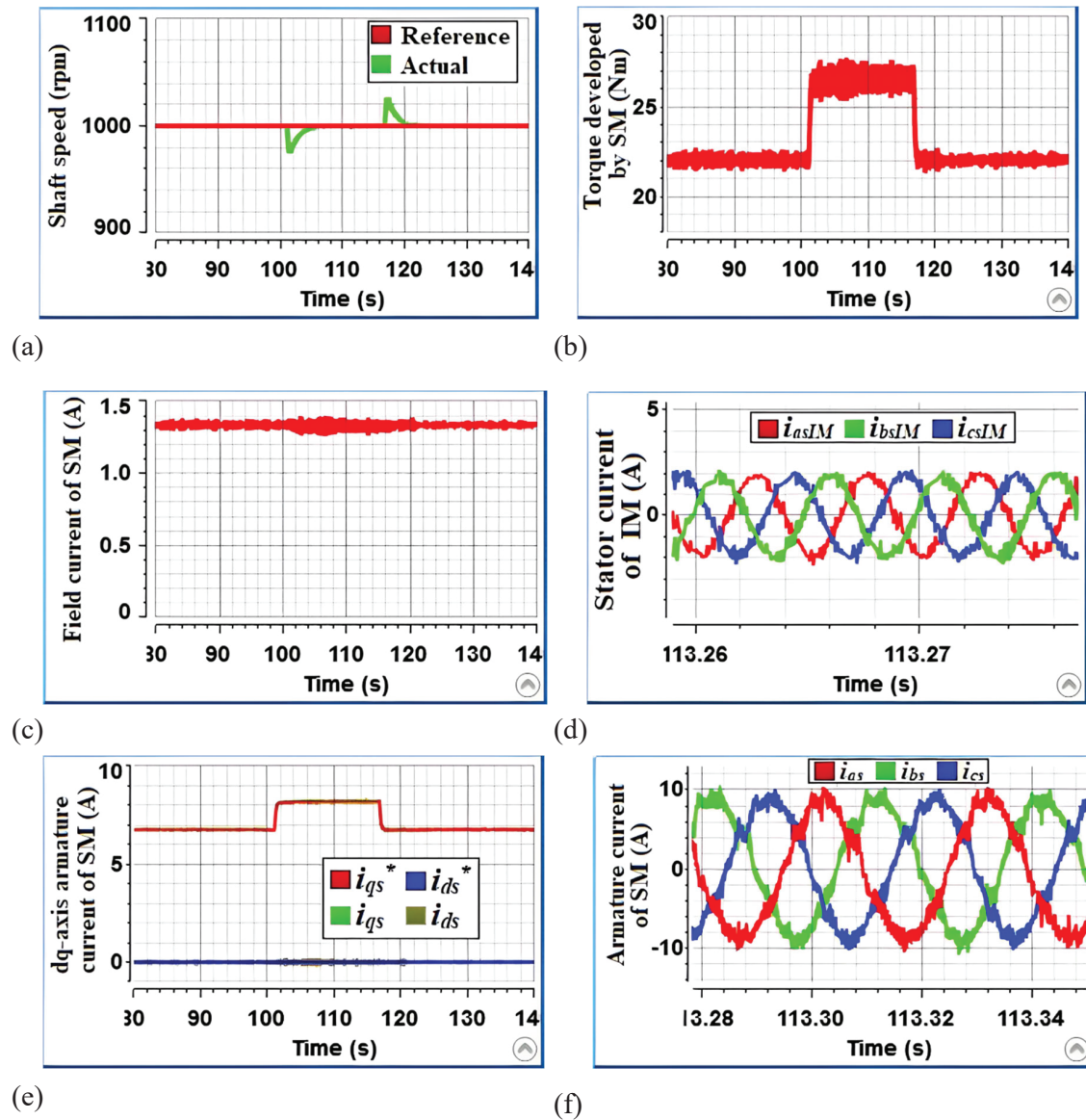


**Figure 11.** Experimental results corresponding to load change from 22 N m to 26.5 N m: (a) shaft speed of BINSYM, (b) torque developed by SM, (c) field current of SM, (d) stator current of IM, (e) dq-axis current of SM, (f) armature current of SM. BINSYM, Brushless Induction excited Synchronous Motor; IM, induction machine; SM, synchronous machine.

## 7. Conclusion

This work has reported a control technique of BINSYM based on MTPA control. The proposed control algorithm aims to reduce the reactive power demand of the exciter and the rms value of armature current of the SM. Out of three different modes, operating the IM in deep-plugging mode is found to be beneficial in lowering its reactive power requirement. A constant slip frequency control (i.e. a frequency of  $-250$  Hz) over the entire speed range has been implemented for the exciter machine. It has been found that the core losses of the exciter machine increase above this frequency without any significant reduction in magnetising current. In case of wound-field SM, there is a flexibility in field current control. In this work, the feature of precise field current control is exploited to achieve maximum torque per ampere operation of the SM. It has been found that field current needs to be kept at its rated value to achieve MTPA when the load torque demand is close to the torque capability. At lighter loads, the reduced value of field current helps in achieving MTPA as opposed to fixed field current operation. Considering the voltage

and current boundary conditions, it has been found that BINSYM is able to produce a torque of 31.6 N·m below base-speed of operation. The overall drive system has been simulated using MATLAB/Simulink under dynamic conditions and the results have been reported. By means of field current regulation, the MTPA can be increased by about 51% for 6 N·m of torque at a speed of 2,800 rpm. It has been found that the motor is able to operate with a CPSR of 2.9. The performance of the machine has been found to be satisfactory in motoring mode of operation. Experiment has been carried out in a prototype machine and the findings closely match the simulation results. Since the proposed drive system is developed using readily available materials and devoid of rare-earth magnets, BINSYM emerges as a better viable option for EV motors.

## References

- Ali, Q., Lipo, T. A. and Kwon, B. (2015). Design and analysis of a novel brushless wound rotor synchronous machine. In: *IEEE International Magnetism Conference (INTERMAG)*. Beijing, China, p. 1.
- Ayub, M., Hussain, A., Jawad, G. and Kwon, B.-I. (2019). Brushless Operation of a Wound-Field Synchronous Machine Using a Novel Winding Scheme. *IEEE Transactions on Magnetism*, 55(6), pp. 1–4. doi: 10.1109/TMAG.2019.2893883.
- Boldea, I., Tutelea, L. N., Parsa, L. and Dorrell, D. (2014). Automotive Electric Propulsion Systems with Reduced or No Permanent Magnets: An Overview. *IEEE Transactions on Industrial Electronics*, 61(10), pp. 5696–5711. doi: 10.1109/TIE.2014.2301754.
- Chakraborty, C. and Bhattacharjee, H. (2023). Synchronous Generator Feeding DC Grid Having Brushless Excitation System With Induction Machine Operating in Deep Plugging Mode. *IEEE Transactions on Industrial Electronics*, 70(12), pp. 11983–11993. doi: 10.1109/TIE.2023.3239931.
- Chakraborty, C. and Rao, Y. T. (2019). Performance of Brushless Induction Excited Synchronous Generator. *IEEE Journal of Emerging and Selected Topics in Power Electronics*, 7(4), pp. 2571–2582. doi: 10.1109/JESTPE.2018.2881068.
- Dai, J., Hagen, S., Ludoi, D. C. and Brown, I. P. (2017). Synchronous Generator Brushless Field Excitation and Voltage Regulation via Capacitive Coupling through Journal Bearings. *IEEE Transactions on Industry Applications*, 53(4), pp. 3317–3326. doi: 10.1109/TIA.2017.2681621.
- Dash, S. K., Medam, V. and Chakraborty, C. (2020). Speed control of brushless induction excited synchronous motor (BINSYM). In: *IEEE International Conference on Power Electronics, Drives and Energy Systems (PEDES)*. Jaipur, India, pp. 1–6.
- Deriszadeh, A., Calasan, M. P., Alaei, A. and Gieras, J. F. (2022). A Novel Field Current Estimation Method for Brushless Wound-Field Synchronous Machine. *IEEE Transactions on Transportation Electrification*, 8(3), pp. 3524–3533. doi: 10.1109/TTE.2022.3162173.
- Fu, X., Qi, Q. and Tan, L. (2019). Design and Analysis of Brushless Wound Field Synchronous Machine with Electro-Magnetic Coupling Resonators. *IEEE Access*, 7, pp. 173636–173645. doi: 10.1109/ACCESS.2019.2957133.
- Kimiabeigi, M., Widmer, J. D., Baker, N. J., Martin, R., Mecrow, B. C. and Michaelides, A. (2016). Three-Dimensional Modelling of Demagnetization and Utilization of Poorer Magnet Materials for EV/HEV Applications. *IEEE Transactions on Energy Conversion*, 31(3), pp. 981–992. doi: 10.1109/TEC.2016.2555786.
- Lee, C. H. T., Hua, W., Long, T., Jiang, C. and Iyer, L. V. (2021). A Critical Review of Emerging Technologies for Electric and Hybrid Vehicles. *IEEE Open Journal of Vehicular Technology*, 2, pp. 471–485. doi: 10.1109/OJVT.2021.3138894.
- Nøland, J. K., Nuzzo, S., Tessarolo, A. and Alves, E. F. (2019). Excitation System Technologies for Wound-Field Synchronous Machines: Survey of Solutions and Evolving Trends. *IEEE Access*, 7, pp. 109699–109718. doi: 10.1109/ACCESS.2019.2933493.
- Park, H.-J. and Lim, M.-S. (2019). Design of High Power Density and High Efficiency Wound-Field Synchronous Motor for Electric Vehicle Traction. *IEEE Access*, 7, pp. 46677–46685. doi: 10.1109/ACCESS.2019.2907800.
- Pellegrino, G., Vagati, A., Guglielmi, P. and Boazzo, B. (2012). Performance Comparison Between Surface-Mounted and Interior PM Motor Drives for Electric Vehicle Application. *IEEE Transactions on Industrial Electronics*, 59(2), pp. 803–811. doi: 10.1109/TIE.2011.2151825.
- Raminosa, T., El-Refaie, A. M., Torrey, D. A., Grace, K., Pan, D., Grubic, S., Bodla, K. and Huh, K.-K. (2017). Test Results for a High Temperature Non-Permanent-Magnet Traction Motor. *IEEE*

- Transactions on Industry Applications*, 53(4), pp. 3496–3504. doi: 10.1109/TIA.2017.2687870.
- Rao, Y. T., Chakraborty, C. and Sengupta, S. (2021). Performance and Stability of Brushless Induction Excited Synchronous Generator Operating in Self-Excited Mode for Wind Energy Conversion System. *IEEE Transactions on Energy Conversion*, 36(2), pp. 919–929. doi: 10.1109/TEC.2020.3023960.
- Wang, R., Liu, W., Meng, T., Jiao, N., Han, X., Sun, C. and Yang, Y. (2022). Rotor Position Estimation Method Of Brushless Electrically Excited Synchronous Starter/Generator Based on Multistage Structure. *IEEE Transactions on Power Electronics*, 37(1), pp. 364–376. doi: 10.1109/TPEL.2021.3100361.
- Wang, Z., Ching, T. W., Huang, S., Wang, H. and Xu, T. (2021). Challenges Faced by Electric Vehicle Motors and Their Solutions. *IEEE Access*, 9, 5228–5249. doi: 10.1109/ACCESS.2020.3045716.
- Wang, Z., Lu, K. and Blaabjerg, F. (2012). A Simple Startup Strategy Based on Current Regulation for Back-EMF-Based Sensorless Control of PMSM. *IEEE Transactions on Power Electronics*, 27(8), pp. 3817–3825. doi: 10.1109/TPEL.2012.2186464.
- Widmer, J. D., Martin, R. and Kimiabeigi, M. (2015). Electric Vehicle Traction Motors without Rare Earth Magnets. *Sustainability of Materials and Technology*, 3, pp. 7–13. doi: 10.1016/j.susmat.2015.02.001.
- Yao, F., An, Q., Gao, X., Sun, L. and Lipo, T. A. (2015). Principle of Operation and Performance of a Synchronous Machine Employing a New Harmonic Excitation Scheme. *IEEE Transactions on Industry Applications*, 51(5), pp. 3890–3898. doi: 10.1109/TIA.2015.2425363.
- Yao, F., An, Q., Sun, L. and Lipo, T. A. (2016). Performance Investigation of a Brushless Synchronous Machine With Additional Harmonic Field Windings. *IEEE Transactions on Industrial Electronics*, 63(11), pp. 6756–6766. doi: 10.1109/TIE.2016.2581759.
- Zhang, X., Jiao, N., Mao, S., Liu, W. and Fan, Y. (2023). Rotor Position Estimation Method Based on Harmonic Signal for a Wound-Field Synchronous Starter/Generator in the Low-Speed Region. *IEEE Transactions on Power Electronics*, 38(4), pp. 4493–4502. doi: 10.1109/TPEL.2022.3230509.